



Supporting Online Material for  
**A Post-Perovskite Lens and  $D''$  Heat Flux Beneath the Central Pacific**

Thorne Lay,\* John Hernlund, Edward J. Garnero, Michael S. Thorne

\*To whom correspondence should be addressed. E-mail: thorne@pmc.ucsc.edu

Published 24 November 2006, *Science* **314**, 1272 (2006)

DOI: 10.1126/science.1133280

**This PDF file includes:**

SOM Text S1 and S2  
Figs. S1 to S17  
References

# A post-perovskite lens and D'' heat flux beneath the central Pacific

Thorne Lay,<sup>1\*</sup> John Hernlund,<sup>2</sup> Edward J. Garnero,<sup>3</sup> Michael S. Thorne<sup>4</sup>

Supporting Online Material

## Supporting Online Text S1: THERMAL MODELING ISSUES

We employ error function profiles only as a rough guide for fitting the geotherms, because it is the only simple two-parameter model that has a straightforward physical basis in transient conductive heat transfer in a convective thermal boundary layer. However, the fitted parameters (Fig. S15) do not exhibit the typical behavior of simple half-space conductive heating, which in the absence of deformation is characterized by a constant temperature drop and an increasing boundary layer thickness with time. Given the robust warming trend from bin 1 to bin 3, it is likely that material is being transported from bin 1 to bin 3, though modified by significant internal deformation. The minimum strain-rate required to influence a conductive boundary layer is roughly the ratio between the thermal diffusivity and the square of the effective boundary layer thickness, or about  $10^{-16} \text{ sec}^{-1}$  for a thermal diffusivity of order  $10^{-6} \text{ m}^2\text{sec}^{-1}$  and boundary layer of order 100 km. For deviatoric stresses on the order of 10 MPa, this requires an effective viscosity significantly less than  $10^{23} \text{ Pa}\cdot\text{sec}$ , which is quite reasonable for the high temperatures expected at the base of Earth's mantle. We also note that heat flux estimates obtained from these fits are not sensitive to the particular form of geotherm used, as any reasonably smooth monotonic profile will be approximately linear between the CMB and the lower discontinuity due to their relatively close proximity. However, when  $\Delta T_{\text{cmb,pPv}}$  is small the fitted profiles (Fig. S14) do not significantly extend into the pPv stability region (particularly for bin 3), suggesting that either the actual geotherm may be considerably more complex than can be constrained by the present data and/or the higher range of values for  $\Delta T_{\text{cmb,pPv}}$  are more plausible.

## Supporting Online Text S2: D" THERMAL CONDUCTIVITY

Estimates of the heat flux determined by geotherm fits to the double-crossing model vary in proportion to the assumed value of thermal conductivity. Unfortunately, the exact value of the total thermal conductivity of rocks at conditions of the D" Region is not well-constrained by either experiment or theory. Thermal conductivity in the deep mantle is expected to be comprised of two parts: one due to phonon conduction and one due to radiative conduction. While phonon conduction is known to be the primary mechanism for heat transfer in dielectric solids at low to modest temperatures, the possible contribution of radiative heat transfer at higher temperatures prevailing in the deep Earth is less certain.

Because the phonon and radiative components are additive, a lower bound for the thermal conductivity is that due to phonon conduction alone, assuming zero contribution from radiative conduction. Comparison of input power and temperature measurements in laser-heated diamond anvil cell experiments (*S1*) provides one of the few direct experimental constraints on phonon conductivity of oxides at CMB pressures, yielding a plausible range for phonon conductivity of MgO and Al<sub>2</sub>O<sub>3</sub> of about 5-12 W/m/K (*S2*). The range of uncertainty is due in part to uncertainties in the particular form of the depth-dependence of phonon conductivity in addition to the ill-constrained temperature of the outermost core, with higher temperatures yielding smaller values of phonon conductivity. These results are in agreement with some thermal relaxation constraints on thermal diffusivity obtained from shock experiments (*S2-4*). Though less certain, theoretical extrapolations of phonon conductivity from lower pressure measurements of thermal diffusivity (*S5-9*) and phonon scattering time scales inferred from infrared reflectivity measurements (*S10, S11*) are compatible with this range of values.

Few constraints exist regarding the radiative conductivity for stable phases at pressures of the lower mantle, although this has long been postulated to become important at high temperatures in Earth's deep interior (*S12*). A large value for radiative conductivity depends upon poor absorption at infrared and near-infrared frequencies, which is strongly affected by the presence of dissolved iron oxides. Experimental measurements of absorption spectra in Fe-bearing upper mantle silicates reveal a broadening of absorption into the infrared with increased temperature that tends to moderate the increased power of radiated energy at high temperatures (*S13, S14*), while enhanced absorption with increasing pressure in some mineral phases (*S15*) has now been demonstrated at pressures up to 80 GPa (*S16*). The saturation of radiative conductivity in olivine at high temperatures at a value of about 2 W/m/K (*S14*) may roughly approximate an upper bound for the behavior of the Earth's entire mantle (*S2*), however, further experimental work is required to better constrain this estimate. On the basis of a high-spin/lowspin transition in ferrous iron at pressures of the D" layer it was recently suggested that the radiative conductivity of silicate perovskite could dramatically increase in the Earth's lowermost mantle (*S17*), however, recent absorption measurements on Fe-periclase require a decrease in radiative conductivity upon passing through the high-spin/low-spin transition, and demonstrate a strongly increasing degree of absorption with increased Fe-content (*S16*). Thus any Fe-rich portions of the lowermost mantle may exhibit a strongly reduced radiative conductivity.

One can also ask whether a strong increase in radiative thermal conductivity is

compatible with the results obtained in this study and the presence of discontinuity structure inside LLSVP. Mantle convection models predict that an increased thermal conductivity with temperature in D" will lead to the formation of thick "mega-plumes," perhaps providing an alternative explanation for LLSVP regions that does not require chemical heterogeneity (S18), although the existence of post-perovskite will tend to suppress this effect by de-stabilizing the lower boundary layer (S19). We note that such a model does not predict the occurrence of discontinuities in the interior of LLSVP, nor does a purely temperature-induced LLSVP explain the anomalous  $\partial V_s/\partial V_p$  behavior of these regions and diminishes the possibility for the presence of post-perovskite in the absence of significant chemical heterogeneity. Additionally, increased thermal conductivity at CMB conditions decreases the magnitude of radial thermal gradients in the lowermost mantle (S20), thus mitigating its effect on CMB heat flow but also further diminishing the possibility for a post-perovskite double-crossing.

Given the sparsity of firm constraints, we suggest that the thermal conductivity of rocks in the D" layer may be conservatively estimated to fall between 5-15 W/m/K, and in our standard heat flux estimates we use a central value of 10 W/m/K (S21). Higher core temperature and/or higher degree of absorption with enhanced Fe-content will favor the lower range of values, such that the heat flux could be smaller than the values we report by a factor of about two. It should be emphasized that these heat flux estimates can be straightforwardly refined if better constraints on the thermal conductivity can be obtained in the future.

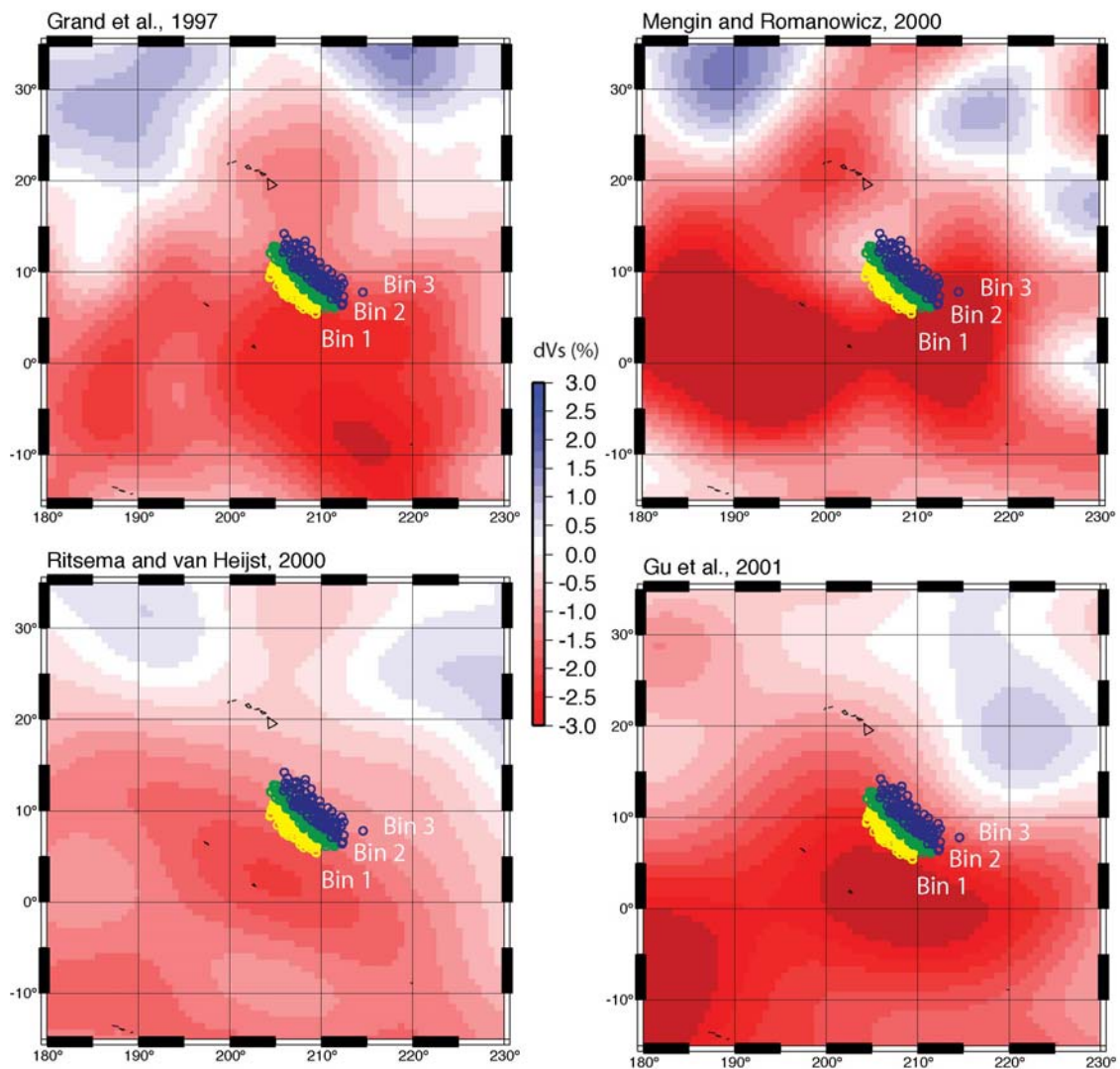


**Fig. S1.** Maps of shear velocity variations in D'' from tomographic models (S22-25) with the ScS CMB reflection point locations for the 3 data bins (as in Fig. 1) superimposed.

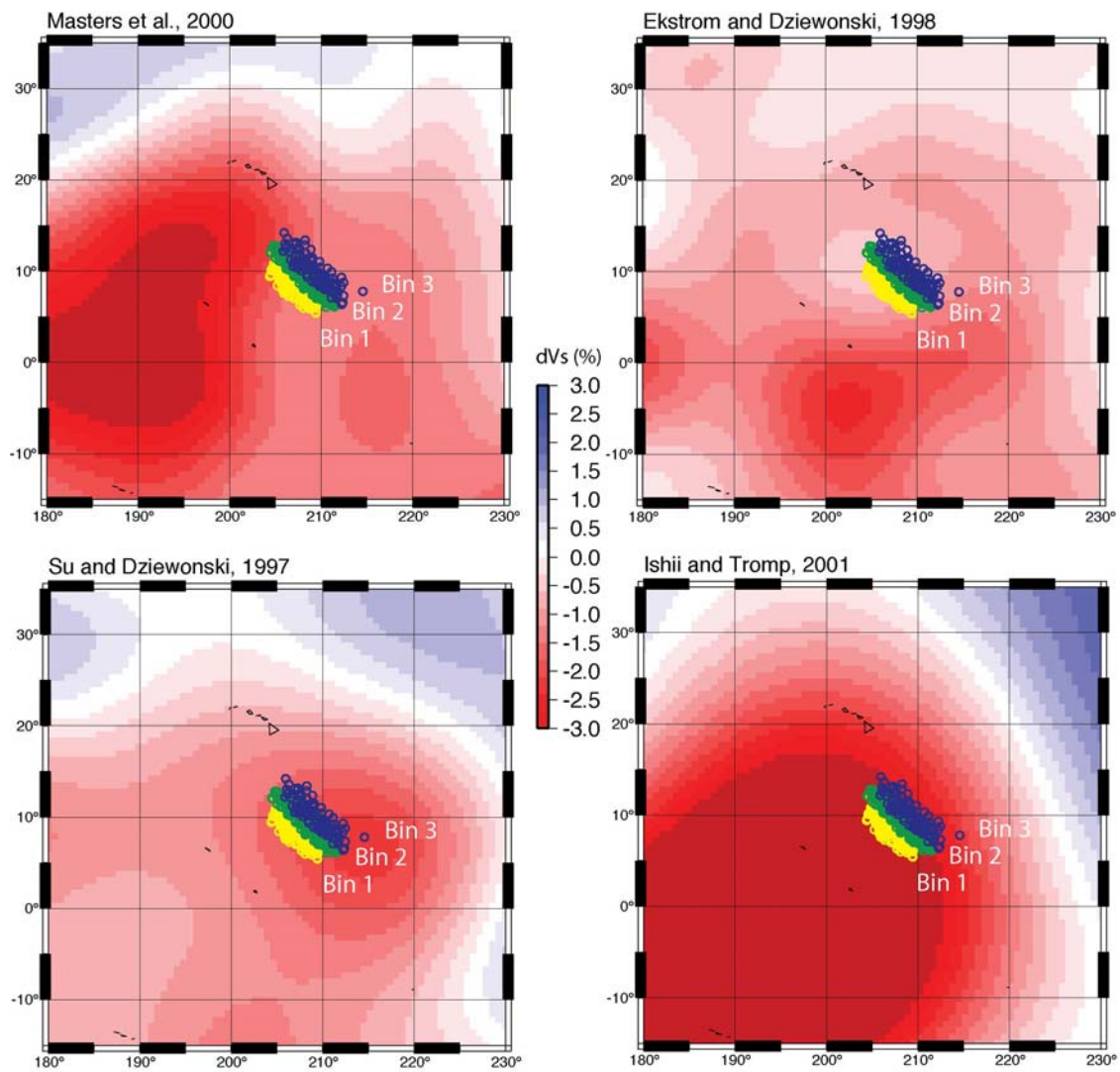


**Fig. S2.** Maps of shear velocity variations in D'' from tomographic models (S26-29) with the ScS CMB reflection point locations for the 3 data bins (as in Fig. 1) superimposed.

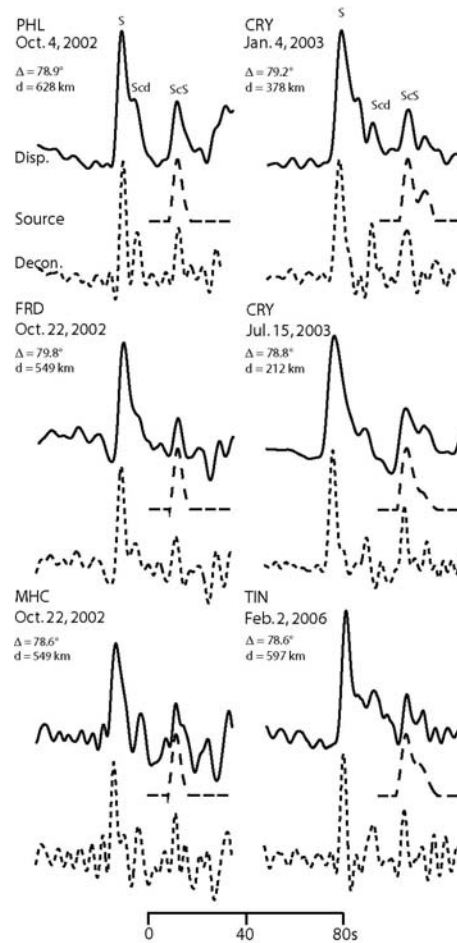


**Fig. S3.** Examples of SH waveforms used in the seismic data analysis. The bold lines indicate recorded broadband ground displacements (Disp.). The station and event information are indicated beside each trace. The epicentral distance ( $\Delta$ ) and source depth ( $d$ ) are also given. The SH waveforms were obtained by deconvolving the horizontal component signals by their instrument responses, and rotating to the radial and transverse components after correction for receiver lithospheric anisotropy (see *S30* for details). The first arrival in each trace is S, and the core-reflection ScS is lined up for all traces. The intermediate arrival (Scd) is a triplication from the  $U_i$  discontinuities, and is sometimes difficult to identify in the raw displacement records because it is not well separated from S. We improve the isolation of Scd by aligning and stacking all clear ScS waveforms for each event to determine an empirical source wavelet (Source – dashed line), which is then deconvolved from the data using a water-level deconvolution, to obtain enhanced bandwidth traces valid for the passband 0.01-0.3 Hz (Decon. – dotted lines). The Scd phase is better isolated in the deconvolved traces, and the recordings from different events can now be stacked together. The records on the left side are for paths that sample Bin 1, which has Scd arrivals close to S. The records on the right side are for paths that sample Bin 2, which has Scd arrivals more centrally located between S and ScS. Additional examples of deconvolution attributes for data used in our stacks are shown in (*S30*, *S31*).

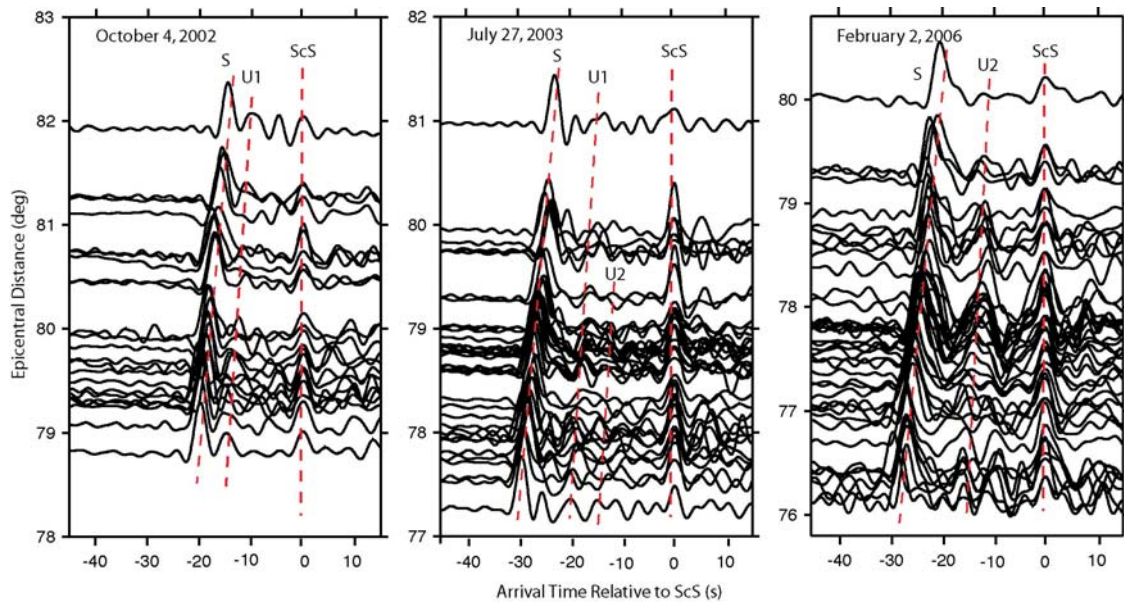


**Fig. S4.** Profiles of deconvolved SH displacements for three Tonga events recorded in California. The traces are aligned on the ScS arrivals with amplitudes normalized on the first arrival, S. Dashed lines indicate the approximate times at which energy from the U1 and/or U2 reflectors should arrive in the seismograms. The event on the left samples Bin1, the event on the right samples Bin 2. The event in the middle has data sampling both bins and there is indication that both U1 and U2 arrivals are present. Robust identification of arrivals between S and ScS, particularly for small negative amplitude features, is not typically possible due to the variability of the signals, station crustal reverberations, and noise. Stacking of the traces is pursued to detect coherent energy in the signals. Additional profiles of data used in this study are shown in on-line supplements to (S30). The events shown here are 3 of 9 new events added to the earlier data collection.

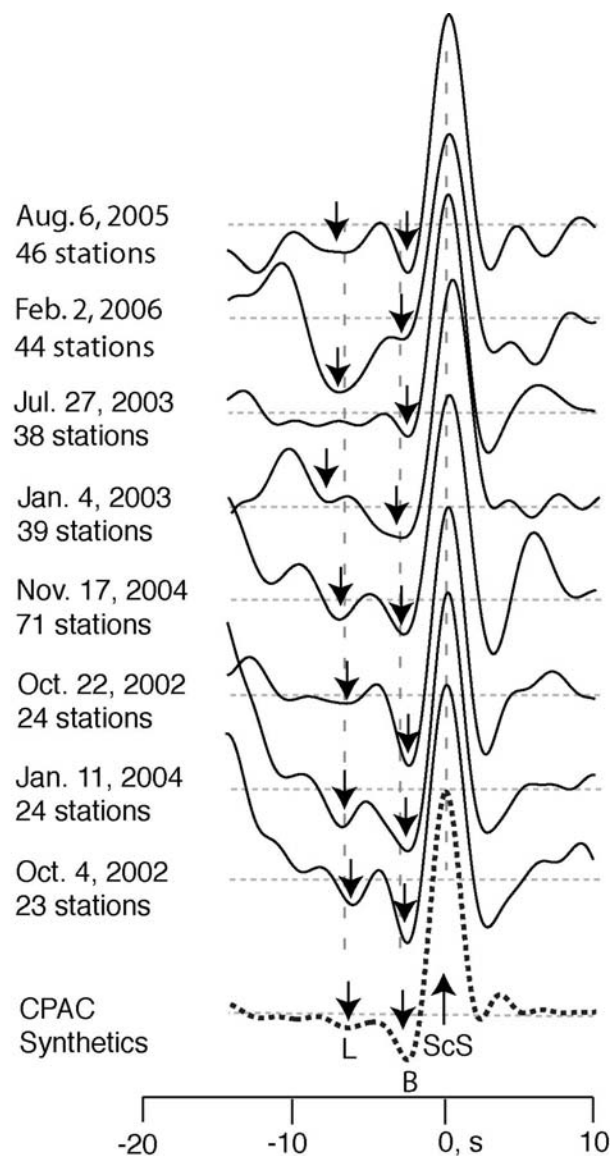


**Fig. S5.** Stacks of all observations for individual events, for the deconvolved SH signals aligned on ScS. The number of stations in each stack is indicated. Two weak negative amplitude arrivals are observed ahead of the positive ScS arrival. At the bottom, synthetics for model CPAC, from (S31), are shown, similarly processed. Model CPAC has two negative velocity jumps in the lowermost 100 km of the mantle, that produce negative amplitude arrivals labeled L and B. Note that individual events show some variability in timing and amplitude of the arrivals; this corresponds to variations in the L and B discontinuities in our 3 Bins. All of these data are new data added for this study. Additional individual event stacks in this format are shown in (S31).

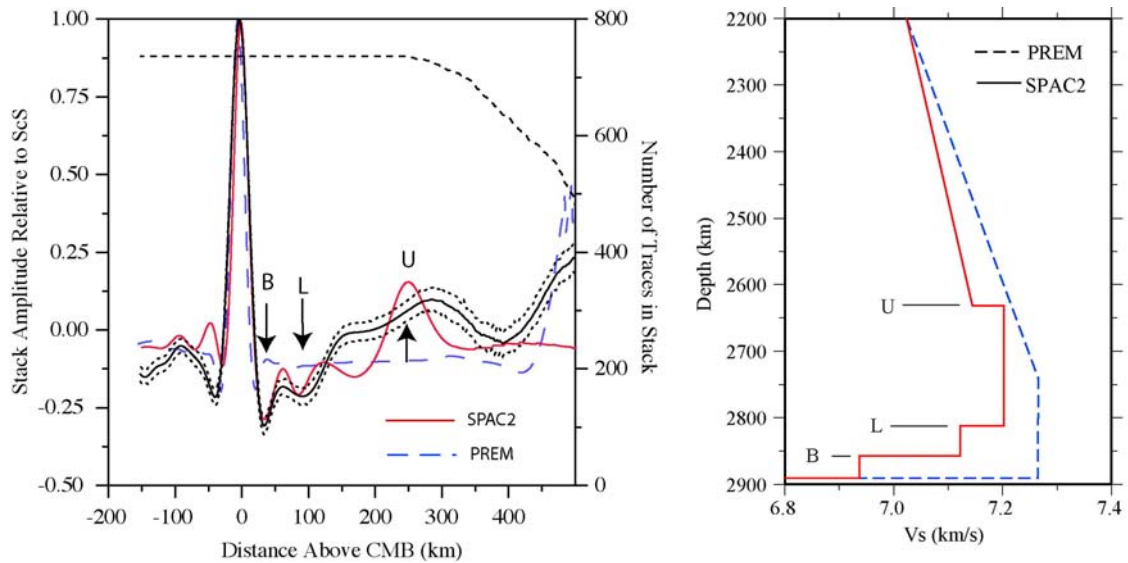


**Fig. S6.** A double-array stack of all 736 seismograms in our final data set is shown on the left (solid black line), along with boot-strap estimates of the 95% confidence interval for the stack (dotted lines). The ScS traces were aligned, and normalized to unity, and then used as reference phases for the double-array stacking. This involves calculating the time difference between ScS and reflection from a target depth in a reference velocity model, then shifting the traces and summing them to determine the strength of any coherent reflected energy from that depth. The possibility of coherent energy after ScS is allowed for by artificially extending the shear velocity at the base of the mantle downward into the core. This allows detection of multiples within lower mantle layers that arrive after ScS, artificially projected to depths below the CMB. The reference velocity model used is model M1, from a regional study of velocity structure under the Central Pacific (*S32*). Synthetics for model PREM (blue lines) and the discontinuity model SPAC2 (red) from (*S30*) are shown. The dashed line and the scale on the right indicate the number of traces in the data stack at each target depth. The PREM and SPAC2 velocity models are shown on the right. The discontinuities produce positive (U) and negative (L, B) reflections with correspondingly labeled peaks in the stacks on the left. Note that the data have a broad distribution of positive energy in the stack from 150 to 400 km above the CMB, which requires lateral variation in the depth of the discontinuity across the region for which data have been combined. Our current total data set is expanded by over 300 waveforms from that used before (*S30*).

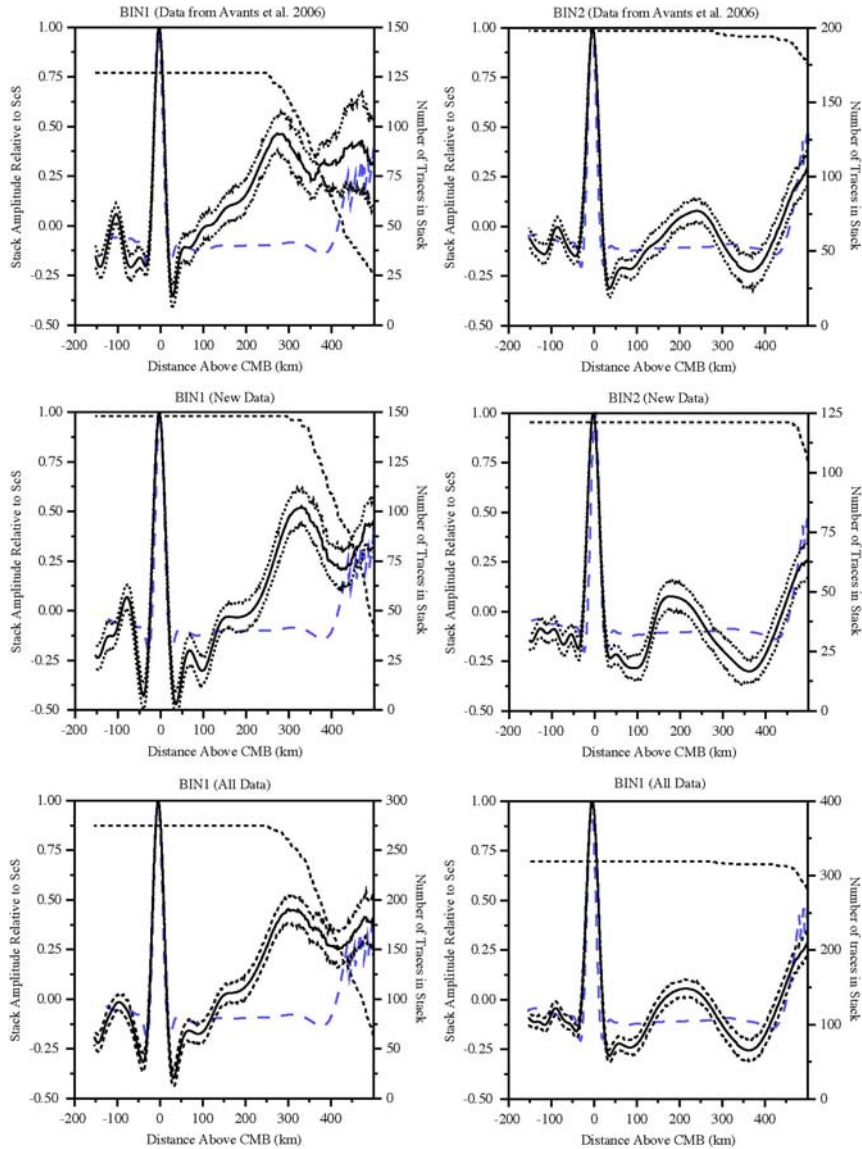


**Fig. S7.** Comparison of double-array stacks for the data sets of (*S30*) in Bin 1 and Bin 2 (top row), for new data added in this study (middle row), and for the final combined data sets (lower row). The data stack and its 95% confidence interval are shown by the solid black lines and dotted bounds, respectively. The number of traces in the stack at each target depth is shown by the dashed line and the scale on the right in each plot. Synthetics for model PREM are shown for reference, as these account for deconvolution and filter side lobes and the contamination from direct S coda that occurs at depths more than 400 km from the CMB. Note that the new data show all of the major features seen in the stacks of data from (*S30*), but there are small shifts in the positions of the peaks near 300 and 200 km. These result from different mean distances to the sources, and are accounted for by making synthetics at the correct distances. The consistency in the stacks, for completely independent data sets, strongly supports the robustness of the observations. The overall stacks, which include almost twice as much data as (*S30*) used, are smooth averages of the total data for each Bin, as desired.

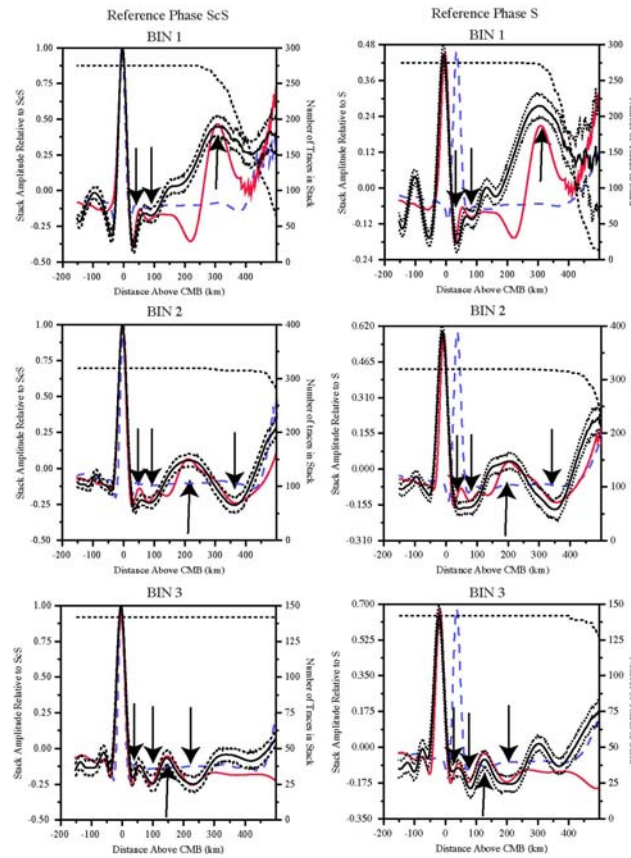


**Fig. S8.** Double array stacks of the final data set sampling Bin1, 2 and 3, comprised of 736 waveforms with uniform bandwidth. The data stacks and 95% confidence intervals are indicated by the solid black lines and dotted lines. The black dashed lines and right-hand scales indicate the number of traces in each stack. Blue dashed curves indicate stacks of PREM synthetics with corresponding distance sampling. Red curves are stacks of synthetics for the final 1-D models for each bin shown in Fig. 2. Significant positive and negative peaks are indicated by the arrows. The left column shows stacks with ScS being the reference phase. The right column shows stacks with S being the reference phase. Model M1 is used as the reference velocity model in all cases. With ScS used as a reference phase, all stacks align on the CMB by definition. With S being the reference phase, the stack amplitudes are now relative to S, and the position of the ScS peak depends on how well the reference model predicts the ScS-S differential times. Note that the data peaks are slightly below the expected CMB location, with increasing discrepancy going from Bin 1 to Bin 3. This behavior is very well predicted by the preferred models. PREM synthetics have a shorter ScS-S time than for model M1, so the apparent ScS position lies above the CMB. The consistency of the stacks and the model fits for different choice of reference phase indicates the robustness of the stacks; every waveform receives different intrinsic weighting by the ScS/S ratios and their variability. Note that the ScS stack amplitude decreases for the stacks in Bin 1 relative to Bin 3 when S is the reference phase. This is due to geometric spreading, and is well-predicted by the models.

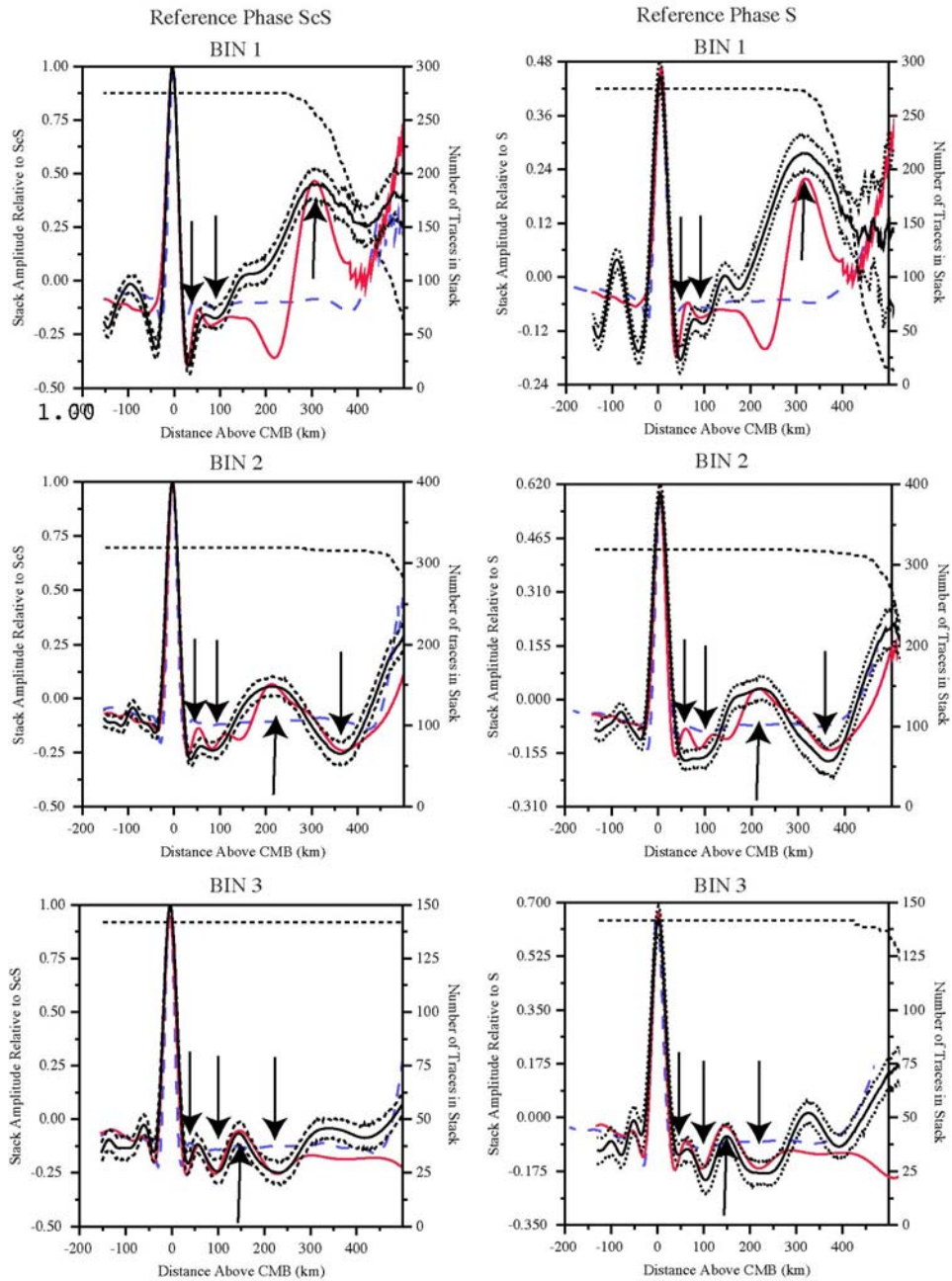


**Fig. S9.** Double array stacks of the final data set sampling Bin1, 2 and 3, comprised of 736 waveforms with uniform bandwidth, as in Fig. S8, except that here the ScS peaks in the stacks relative to S are all artificially aligned on the CMB. This helps to evaluate the similarity between stacks for different reference phases and from bin to bin. All plot features are otherwise the same as in Fig. S8.

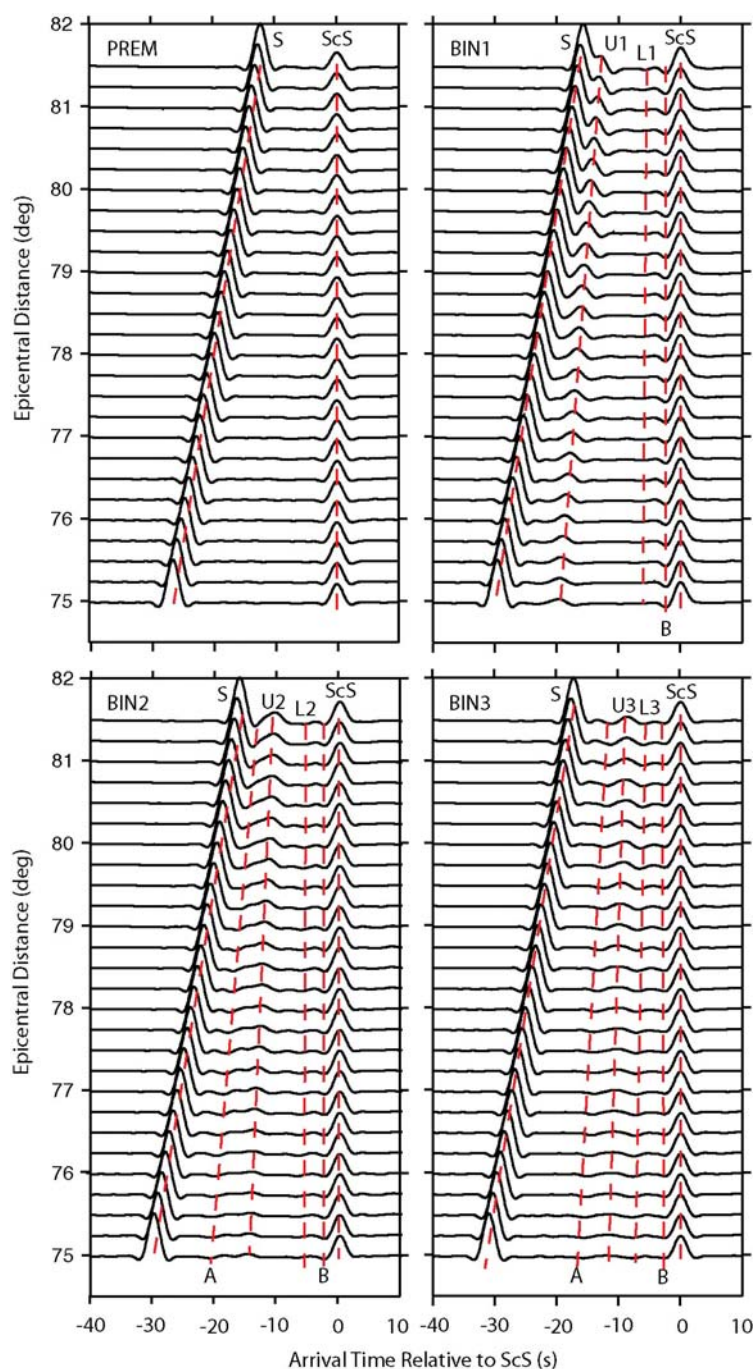


**Fig. S10.** Profiles of synthetic SH seismograms computed by the reflectivity method for models PREM, and the final 1D fits to Bin 1, 2, and 3. The traces are all aligned on ScS, and intermediate arrivals from discontinuities A, U, L, and B (Fig.1 2) are indicated. The relatively small size of velocity discontinuities in the models gives rise to very weak negative amplitude features and stronger positive amplitude features. This asymmetry is due to triplication for velocity increases versus pre-critical reflection for velocity decreases (S33). We rely on comparison of stacks of synthetics to stacks of data in order to confidently determine the velocity structure.

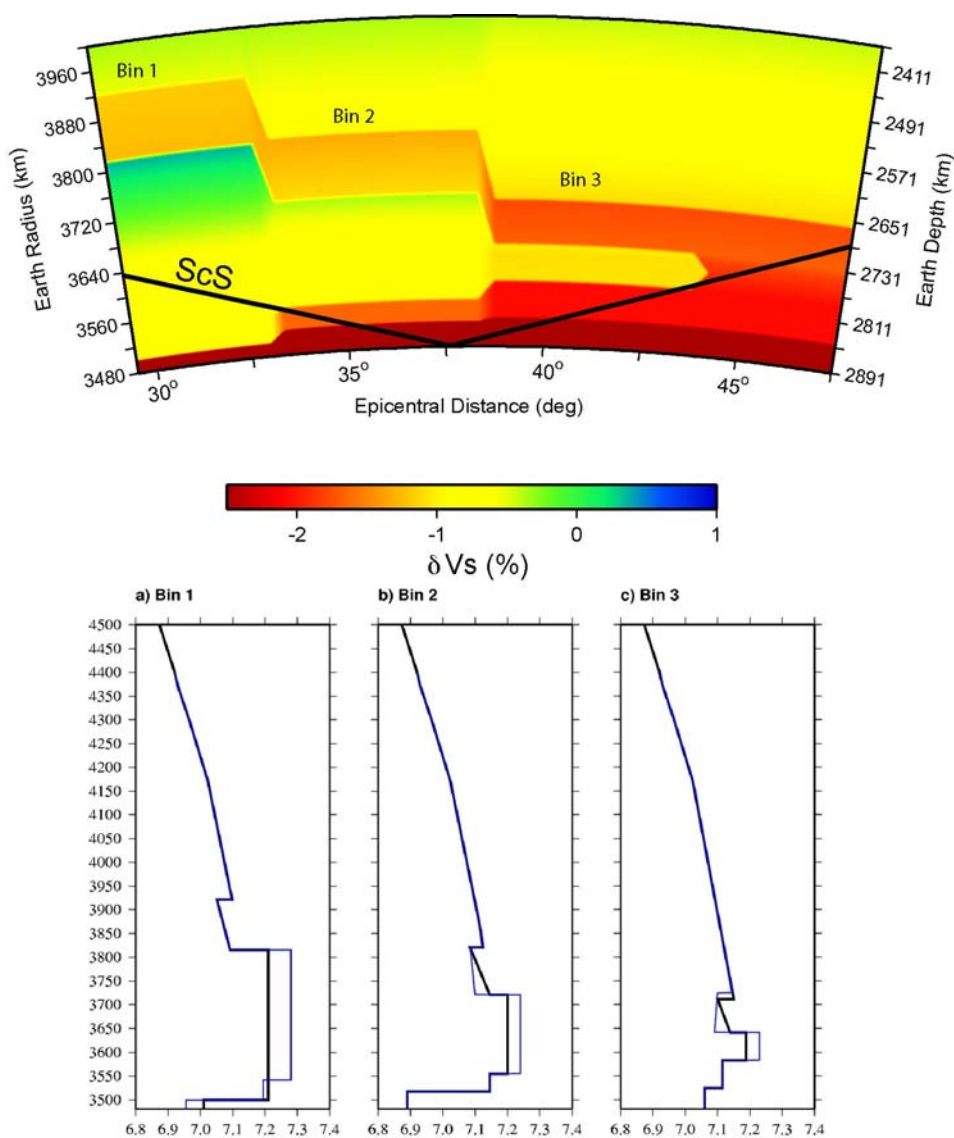


**Fig. S11.** (Top) Cross-section through a 2.5D (axi-symmetric spherical) shear velocity model found to be compatible with the Bin 1, Bin 2 and Bin 3 data stacks. The average radial structure in each portion of the model is shown below, with the bins labeled according to the data subdivision. The width of each domain is about  $5^\circ$ , and must be larger than  $4^\circ$  to match the data. The velocity profiles compare the preferred 1D models (black lines) found from modeling the data set of (*S30*), compared to the 2.5D velocities (blue lines). The velocities in the high velocity layer increase in the laterally varying model due to the asymmetry of structure sampled by the grazing waves (see the ScS raypath at the top). The velocity increase matches both the timing and amplitude of the triplications from the positive discontinuities. Axi-symmetric spherical model finite-difference computations were used to compute the SH responses for this model, for periods as short as 3 s, and the synthetics were processed the same way as the data, double-array stacked, and compared to the data.

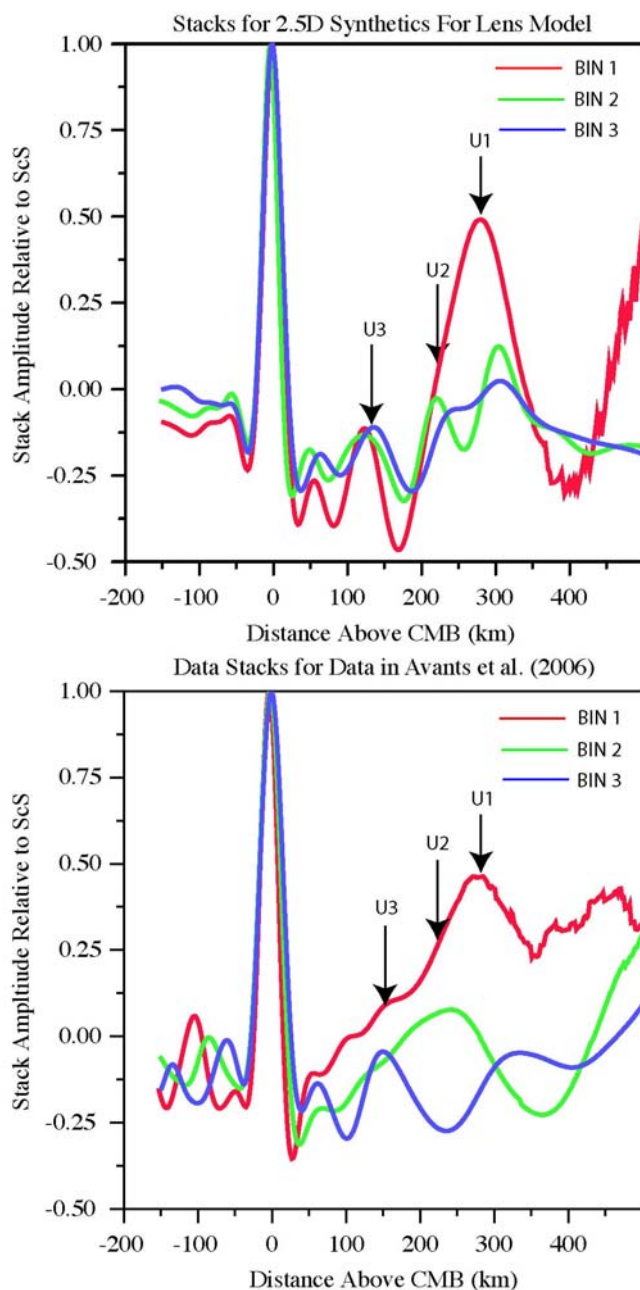


**Fig. S12.** Double-array stacks of synthetics for the 2.5D model in Fig. S11 (top) and the subset of data from (*S30*) (bottom). The data and synthetics for each bin are colored consistently, and the positive peaks produced by triplications from the  $U$  velocity increases are indicated by arrows. The model successfully matches the strong change in stacks from Bin1 to Bin 2 to Bin 3, and fits the basic features of the data stacks, but does not predict persistence of the post-critical diffractions from the discontinuities to larger distances than observed (note the energy near 300 km depth for the Bin 2 and Bin 3 synthetics). Irregularity in the boundaries and three-dimensionality of the lens structure is likely responsible, but the constraints on the 3-D structure are not sufficient to undertake much more extensive modeling at this time.

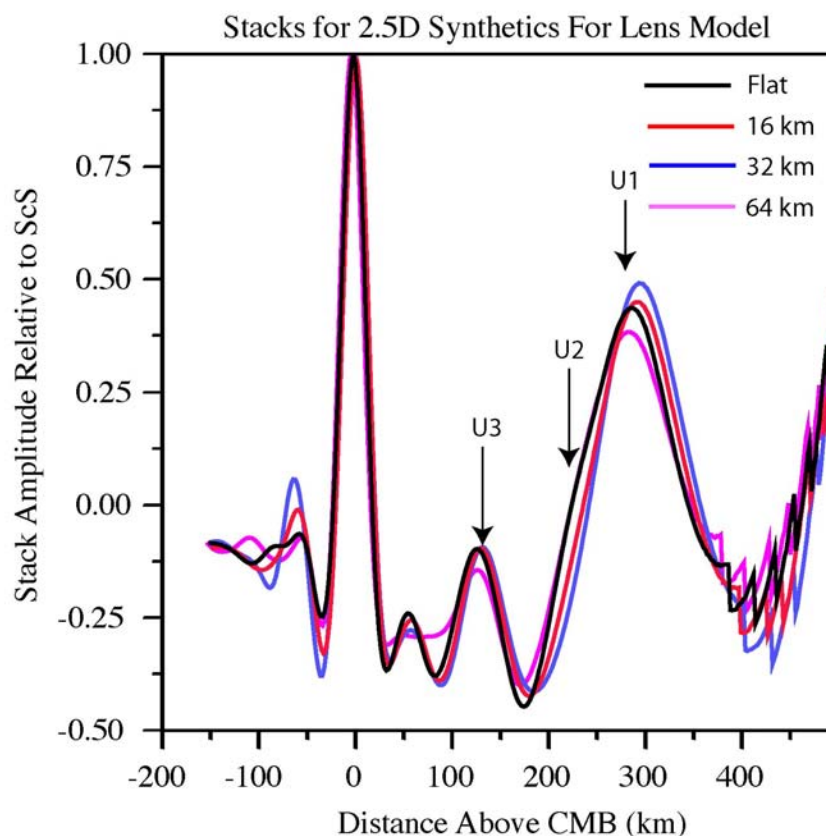


**Fig. S13.** Double-array stacks of synthetics for Bin 1 in the 2.5D Lens model with all discontinuities in the structure being given sinusoidal topographic variations with specified peak amplitudes (indicated by colors) with various wavelengths; in this case  $9.6^\circ$  for the 16 and 32 km amplitudes, and  $2.4^\circ$  for the 64 km amplitudes. Due to the grazing nature of the wave field, the sensitivity to topography is limited, as extensive lateral averaging of the structure occurs. However, these synthetics demonstrate that the variability in data stacks can plausibly be attributed to unresolved small-scale structure in the lens.

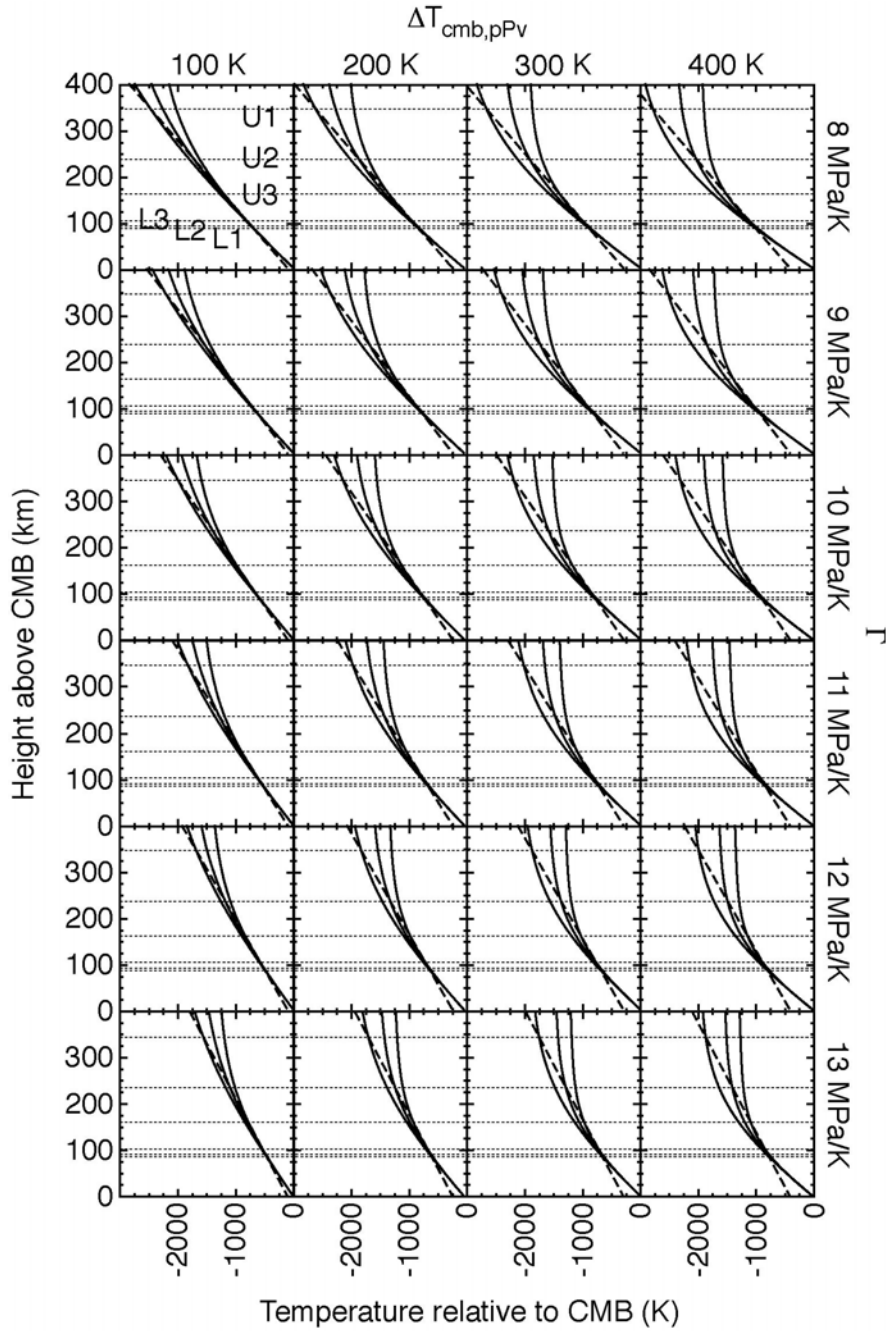


**Fig. S14.** Supplement to Figure 3, showing additional thermal model fits to the Central Pacific discontinuity observations for the indicated values of Clapeyron slope,  $\Gamma$ , and  $\Delta T_{\text{cmb,pPv}}$ . The equation used to fit the geotherms is  $T = T_{\text{cmb}} - (r - r_{\text{cmb}}) \cdot (dT/dr)_{\text{adiab}} - \Delta T_{\text{tbl}} \cdot \text{erf}[(r - r_{\text{cmb}})/\delta]$ .  $T_{\text{cmb}}$  is the temperature at the CMB, at radius,  $r = r_{\text{cmb}}$ .  $(dT/dr)_{\text{adiab}}$  is the adiabatic, thermal gradient, taken as 0.25K/km (S34).  $\Delta T_{\text{tbl}}$  is the thermal boundary layer temperature contrast.  $\delta$  is the thickness of the thermal boundary layer. Fig. S15 gives the values found for the latter two parameters for every solution.

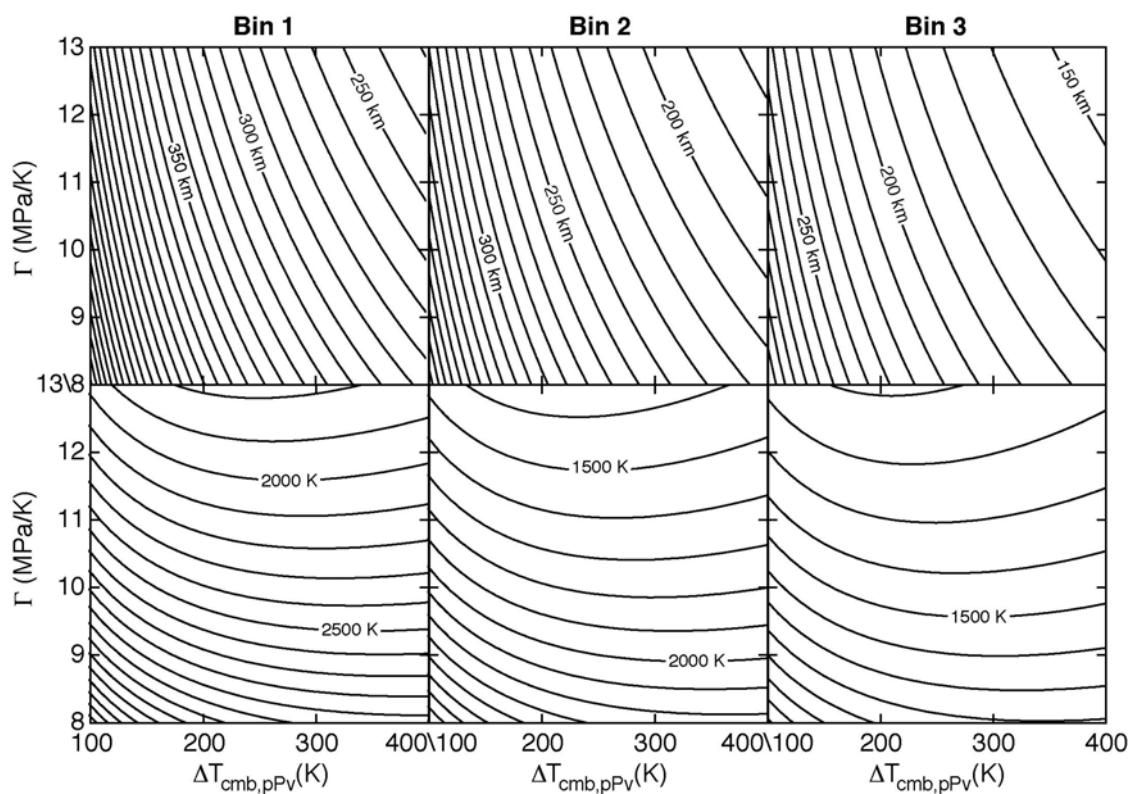


**Fig. S15.** Parameters of the thermal models that match the observed discontinuity depths as function of Clapeyron slope,  $\Gamma$ , and  $\Delta T_{\text{cmb,pPv}}$ . The top row shows the thermal boundary layer thickness for each combination of parameters for each of the three data bins. The bottom row shows the total radial temperature increase across the thermal boundary layer for each case.

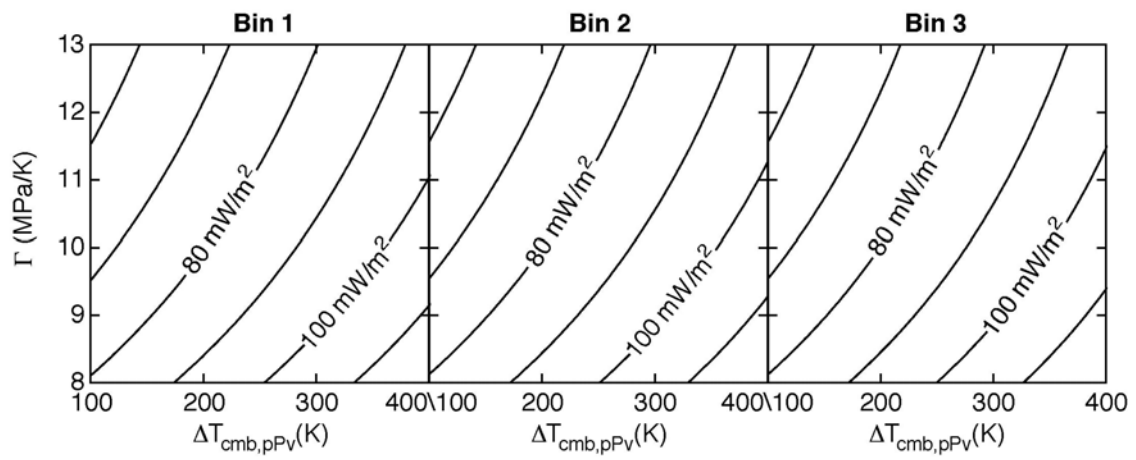


**Fig. S16.** Heat flux predictions as a function of Clapeyron slope,  $\Gamma$ , and  $\Delta T_{\text{cmb,pPv}}$  for models that fit each Bin independently. Very little variation in heat flux is found.

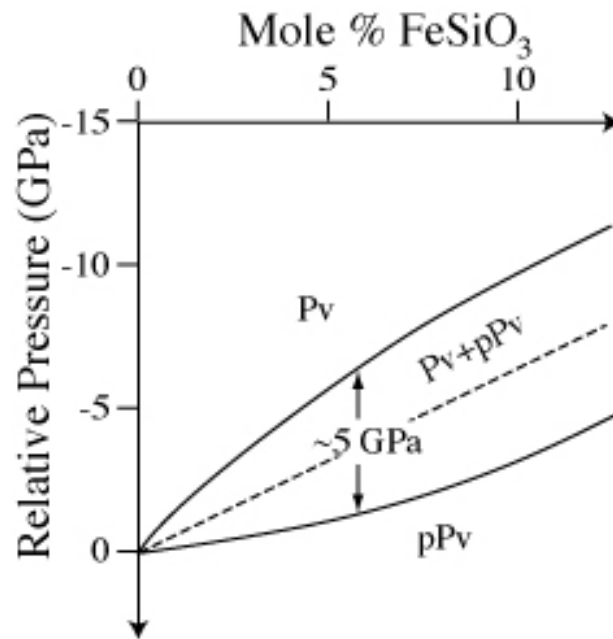


**Fig. S17.** Schematic effect of mole % Fe on the pPv-Pv phase boundary. A phase boundary shift of about 6 GPa is required between the Central Pacific and Cocos Plate regions for the hypothesis of an Fe-rich chemical pile.

## Supporting Online Material References

- S1. S. K. Saxena, G. Shen, P. Lazor, *Science* **264**, 405 (1994).
- S2. M. Manga, R. Jeanloz, *J. Geophys. Res.* **102**, 2999 (1997).
- S3. J. D. Bass, B. Svendsen, and T. J. Ahrens, in *High Pressure Research in Mineral Physics, Geophys. Monogr. Ser.*, 39, M. H. Manghnani, Y. Syono, Eds., (American Geophysical Union, Washington, DC, 1987), pp. 149-154.
- S4. H. Tan, T. J. Ahrens, *High Pressure Res.* **2**, 145 (1990).
- S5. H. Fujisawa, N. Fujii, H. Mizutani, H. Kanamori, S. Akimoto, *J. Geophys. Res.* **75**, 4727 (1968).
- S6. S.W. Keiffer, *J. Geophys. Res.* **81**, 3025 (1976).
- S7. S. Maj, *Pure Appl. Geophys.* **116**, 1225 (1978).
- S8. M. Osako, E. Ito, *Geophys. Res. Lett.* **18**, 239 (1991).
- S9. T. Katsura, *Phys. Earth Planet. Int.* **101**, 73 (1997).
- S10. A. M. Hofmeister, *Amer. Mineral.* **86**, 1188 (2001).
- S11. A. M. Hofmeister, *Science* **283**, 1699 (1999).
- S12. S. P. Clark, *Amer. Mineral.* **43**, 732 (1957).
- S13. Y. Fukao, H. Mizutani, S. Uyeda, *Phys. Earth Plan. Int.* **1**, 57 (1968).
- S14. T. J. Shankland, U. Nitsan, A. G. Duba, *J. Geophys. Res.* **84**, 1603 (1979).
- S15. H.-K. Mao, P. M. Bell, *Science* **176**, 403 (1972).
- S16. A. F. Goncharov, V. V. Struzhkin, S. D. Jacobsen, *Science* **312**, 1205 (2006).
- S17. J. Badro, et al., *Science* **305**, 383 (2004).
- S18. C. Matyska, D. A. Yuen, *Phys. Earth Plan. Int.* **154**, 196 (2006).
- S19. C. Matyska, J. Moser, D. A. Yuen, *Earth Planet. Sci. Lett.* **125**, 255 (1994).
- S20. A.P. van den Berg, D. A. Yuen, J. R. Allwardt, *Phys. Earth Planet. Int.* **129**, 359 (2002).
- S21. F. Stacey, *Physics of the Earth*, (Brookfield, Kenmore, Queensland, ed. 3, 1992).
- S22. S. P. Grand, R. D. van der Hilst, S. Widiyantoro, *GSA Today* **7**, 1 (1997).
- S23. C. Mégnin, B. Romanowicz, *Geophys. J. Int.* **143**, 709 (2000).
- S24. J. Ritsema, H. J. van Heijst, *Sci. Prog.* **83**, 243 (2000).
- S25. Y. J. Gu, A. M. Dziewonski, W. J. Su, G. Ekström, *J. Geophys. Res.* **106**, 11169 (2001).
- S26. G. Masters, G. Laske, H. Bolton, A. M. Dziewonski, in *Earth's Deep Interior: Mineral Physics and Tomography From the Atomic to the Global Scale*, S. Karato, A. M. Forte, R. C. Liebermann, G. Masters, L. Stixrude, Eds., (American Geophysical Union, Washington, D.C., 2000), pp. 63-88.
- S27. G. Ekström, A. M. Dziewonski, *Nature* **394**, 168 (1998).
- S28. W. J. Su, A. M. Dziewonski, *Phys. Earth Planet. Int.* **100**, 135 (1997).
- S29. M. Ishii, J. Tromp, *Geophys. J. Int.* **145**, 77 (2001)
- S30. M. Avants, T. Lay, S. A. Russell, E. J. Garnero, *J. Geophys. Res.* Vol. **111**, B05305, doi:10.1029/2004JB003270 (2006).
- S31. M. Avants, T. Lay, E. J. Garnero, *Geophys. Res. Lett.* Vol. **33**, L07314, doi:10.1029/2005GL024989 (2006).
- S32. J. Ritsema, E. J. Garnero, and T. Lay, *J. Geophys. Res.* **102**, 20,395-20,411 (1997).
- S33. C. Flores, T. Lay, *Geophys. Res. Lett.* **32**, L24305, doi:10.1029/2005GL024366 (2005).
- S34. J. M. Brown, T. J. Shankland, *Geophys. J. R. Astron. Soc.* **66**, 579 (1981).